Postprint version of the paper by Walker et al., in J. Mater. Chem. C. vol. 8, Iss. 9, pg. 3206-3216
Doi.org/10.1039/C9TC06918F

Super-coercive electric field hysteresis in ferroelectric plastic crystal tetramethylammonium bromotrichloroferrate(III)

Julian Walker[a], Rany Miranti[a], Susanne Linn Skjærvø[a], Tadej Roja[cb], Tor Grande[a], Mari-Ann Einarsrud[a]

[a.] *Department of Materials Science and Engineering, NTNU Norwegian University of Science and Technology, Trondheim, Norway*
[b.] *Electronic Ceramics Department, Jozef Stefan Institute, Ljubljana, Slovenia*

Ionic plastic crystals are part of an emerging class of hybrid organic-inorganic ferroelectrics. The combination of low dielectric constants (<20), strong piezoelectric coefficients (>100 pC/N) and low temperature synthesis make ferroelectric plastic crystals strong candidates for sensing and energy harvesting applications so more research of the electrical properties, such as dielectric loss and super-coercive hysteresis is needed. Tetramethylammonium bromotrichloroferrate(III) was studied as a prototypical material and a non-centrosymmetric orthorhombic Amm2 structure was confirmed by X-ray diffraction at room temperature. The relative permittivity was below 20 at high frequencies (105 Hz) but high dielectric losses at frequencies <103 Hz caused the permittivity to increase. The bulk material showed super-coercive hysteresis with remanent polarizations of 3.8 μC/cm2 and peak-to-peak strains of 0.046 %. The coercive field and peak-to-peak strain exhibited frequency dependence, reducing from >80 to 30 kV/cm and 0.046 to 0.017 % respectively between 100 and 0.1 Hz. At 100 Hz the material exhibited a strong asymmetric hysteresis that was reversible depending on the electric field direction. The observed behavior was consistent with a defect pinning model of ferroelectric switching behavior and thus some likely point defect species were proposed and thought to result from solution non-stoichiometry or residual moisture and solvent.

Introduction

Ferroelectric materials with switchable spontaneous electrical polarizations, piezoelectric coefficients and useful dielectric responses play an important role in electronics such as capacitors, transducers, sensors and actuators.[1–3] Currently, most commercial ferroelectrics are metal oxides, such as $BaTiO_3$ and $Pb(Zr_{(1-x)}Ti_x)O_3$ (PZT). However, a technological push towards flexible electronics and novel functionality, together with a drive to explore more sustainable material alternatives that use fewer elements from the periodic table and have lower energy budgets, is stimulating investigation of new ferroelectric materials beyond the metal oxide-based systems.[4–6] As a result, some hybrid organic-inorganic and supramolecular materials have become interesting candidates for new ferroelectric materials. [7–11]

Recently, materials known as plastic crystals have emerged with a technologically significant combination of dielectric, ferroelectric and piezoelectric properties at room temperature.[7–10] Plastic crystals are supramolecular materials consisting of arrays of ions or neutral molecules that form the crystal lattice.[12,13] They are characterized by the presence of an intermediate solid-liquid phase at elevated temperatures, a so called mesophase, in which the molecular centers of mass occupy fixed positions in the crystal lattice while exhibiting high rotational freedom. In this structural state the material can be easily plastically deformed. The plasticity is advantageous as it enables individual crystals to be pressed together to form polycrystalline ceramic-like materials without the need for high-temperature densification.[9] Polycrystalline ferroelectric plastic crystals can be poled using external electric fields, producing materials with useful macroscopic properties, such as piezoelectricity, at a fraction of the process temperatures required for metal

oxides.[5,8,9,14] For example, plastic crystal tetramethylammonium bromotrichloroferrate(III) ($[N(CH_3)_4][FeBrCl_3]$) requires process temperatures of <150 °C, while $BaTiO_3$ requires approximately 1100 °C to obtain a dense ceramic. The unique combination of plasticity at accessible temperatures and ferroelectricity at room temperature makes plastic crystal ferroelectrics a promising emerging class of functional materials that may prove to be useful alternatives for metal oxides in selected applications.

$[N(CH_3)_4][FeBrCl_3]$ is a ferroelectric with a piezoelectric coefficient (d_{33}) of 110 pC/N and a dielectric constant (ε_r) below 20 at 10^6 Hz (1 MHz).[9] With this combination of properties $[N(CH_3)_4][FeBrCl_3]$ may be a strong candidate for application in energy harvesting devices or sensors, and notably the piezoelectric coefficient exceeds that of the most commercially successful organic ferroelectrics to date, the poly-vinyl fluoride (PVDF)-based systems (d_{33} usually <40 pC/N).[15,16] The temperature dependent crystal structure of $[N(CH_3)_4][FeBrCl_3]$, and the related material with $[FeCl_4]^-$ ions, is well characterized with a total of five polymorphs as a function of temperature below the melting point. Two ferroelectric phases exist between -10 and 75 °C, two paraelectric phases below and above this range and a mesophase above 110 °C.[9,17–20] However, initial reports of the ferroelectric properties have emerged only recently.[9] As a result, detailed studies of the electromechanical properties, ferroelectric/ferroelastic domain switching and effects of electrical leakage have not been widely reported. The ferroelectric properties of $[N(CH_3)_4][FeBrCl_3]$ therefore require further attention in order to shed light on the underlying mechanisms and the functional properties of this intriguing family of plastic crystal ferroelectrics.

In this work we provide a look at the room temperature structure and dynamics of polycrystalline $[N(CH_3)_4][FeBrCl_3]$ with X-ray diffraction, Raman and infrared (FTIR) spectroscopy, and study the frequency and electric field dependent electrical and electromechanical properties. The super-coercive electric field data provide insight into the hysteresis behavior of $[N(CH_3)_4][FeBrCl_3]$ that is relevant for understanding the functional properties and mechanisms involved with ferroelectric switching in the wider family of plastic crystal ferroelectrics.

Experimental

Crystals of $[N(CH_3)_4][FeBrCl_3]$ were synthesized using reagent grade tetramethylammonium bromide (99 %, Sigma Aldrich) and iron(III) trichloride hexahydrate (98 %, Sigma Aldrich). Reagents were dissolved separately in deionized water at room temperature before being mixed together with a magnetic stirrer for 10 min. The solution was dehydrated with a rotary evaporator at 70 °C and a vacuum beginning at 150 mbar and decreasing to 70 mbar for approximately 60 min. The dehydrated dark red agglomerates remaining were then added to 200 mL of ethanol (99.999 %, Sigma Aldrich) and heated to 70 °C for 15 min while being mixed. Once all solids were dissolved the solution was cooled to room temperature under ambient conditions for 24 h. The resulting crystals were separated from the solution using vacuum filtration and dried on a hot plate for 30 min at 50 °C. Samples for microstructural comparison were produced by drying crystals in a vacuum oven at 60 °C for 6 h.

The crystals were pressed into polycrystalline free-standing (meaning no substrate) thick films by uniaxially pressing 0.3 g charges of crystals at 150 °C and a pressure of 12 MPa for 15 min. The pressure was released at 150 °C and samples were removed to a bench top to cool to room temperature under ambient conditions. Aluminum foil was used as a buffer layer on each side of the crystals between two stainless-steel plates. Microstructural characterization was performed with a low voltage scanning electron microscope (LVSEM) Hitachi S-3400N. A D8 focus X-ray diffractometer with a Cu source was used for structural analysis collecting a diffraction pattern between 5 and 70° 2θ with 0.0199 ° steps and an acquisition time of 2 s per step. The dendrite crystals were crushed prior to X-ray diffraction (XRD) measurement to minimize preferential

orientation during powder packing, and pressed pellets were measured whole. XRD fitting was performed with Bruker AXS Topas® software package fitting the *Amm*2 phase from Cambridge crystallographic data center (CCDC) file 1574204 from Harada et al.[9] Atomic site positions were fixed to literature values. A preferred orientation factor using an eighth order spherical harmonic and a Steven's strain factor function for orthorhombic structures were both utilized in the refinement.

Renishaw InVia Reflex spectrometer system with the excitation wavelength of 532 nm and a power of 1 mW was used for Raman spectroscopy. The laser was focused onto the sample with a 100× magnification of the optical lens with spectral resolution less than 1 cm^{-1}. Bruker vertex 80V infrared spectroscopy system was used for infrared (FTIR) spectroscopy by attenuated total reflection (ATR) method.

For electrical measurements, 3 mm diameter gold electrodes were sputter coated through a shadow mask onto 300 µm thick, 10 mm^2 samples. Dielectric capacitance and loss were measured with Hewlett Packard LCR meter 4142. Ferroelectric switching measurements were performed with an Aixacct ferroelectric tester with a Trek 10 kV signal amplifier and a laser interferometer for strain measurement. A triangular waveform was used for all measurements and the field was increased in 10 kV/cm intervals. For these measurements an insulating oil was avoided as the long- and short-term effects of the oil on the $[N(CH_3)_4][FeBrCl_3]$ material were unknown. This resulted in some arcing during measurement which contributed to noise in the current signal.

Results and discussion

Crystal structure and microstructure

From the powder XRD pattern collected at room temperature the structure of $[N(CH_3)_4][FeBrCl_3]$ was identified as orthorhombic with the non-centrosymmetric space group *Amm*2, in agreement with the literature (Fig. 1a).[9,17–20] By allowing the ethanol-based solution to cool to room temperature under ambient conditions the crystal growth occurred dendritically, producing elongated branched crystals on the order of 50 µm in diameter and 500 µm long (Fig. 1b). Refinement of the *Amm*2 structure to the XRD profile from crushed crystals produced a goodness of fit (GOF) of 2.86 and lattice parameters of a=7.2223 Å, b=8.9881 Å and c=9.3116 Å.

$[N(CH_3)_4][FeBrCl_3]$ has a cesium chloride-type crystal structure where the organic $[N(CH_3)_4]^+$ and inorganic tetrahedral $[FeBrCl_3]^-$ molecular ions occupy the two sites in the crystal lattice (Fig. 1c).[9,17-20] The resulting structure has distinct planes of molecular species visible along <010> and <001>. The inorganic anions and organic cations each fill a large three-dimensional space with the symmetry and volume of the molecular ions giving rise to unit cell parameters on the order of 10 Å and to the molecules being described as, so-called globular molecular ions best visualized by space filling the ionic volumes in the structural model (Fig. 1d). The globular molecules in the $[N(CH_3)_4][FeBrCl_3]$ give rise to the mesophase above 110 °C, as the molecular centers of mass can maintain a long-range order in the crystal structure while their orientation displays high degrees of rotational freedom and creates local disorder. Although both $[N(CH_3)_4][FeBrCl_3]$ and the organo-

Postprint version of the paper by Walker et al., in J. Mater. Chem. C. vol. 8, Iss. 9, pg. 3206-3216
Doi.org/10.1039/C9TC06918F

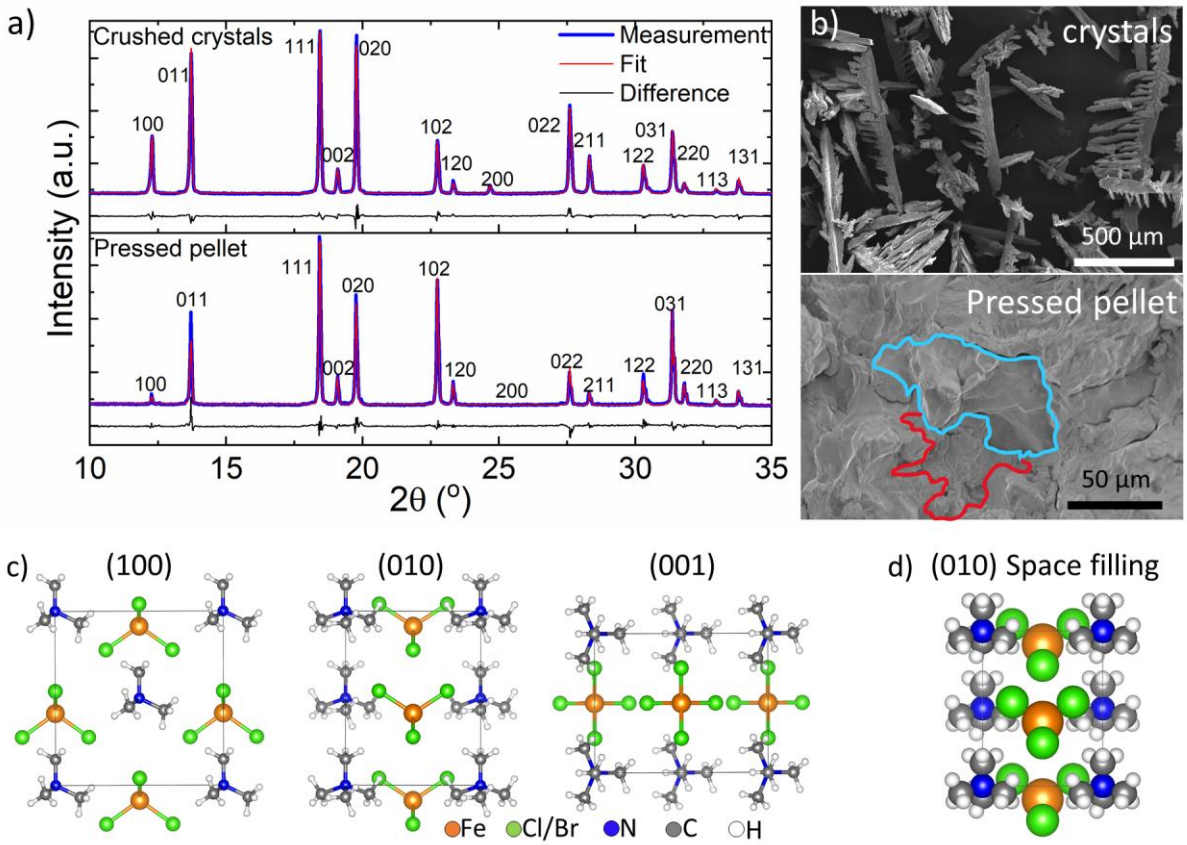

Fig. 1. a) XRD pattern, data fit and residual difference profiles of crushed crystals and pressed pellets of [$(CH_3)_4N$][$BrCl_3Fe$]. Peaks are labelled according to Amm2 orthorhombic space group hkl values. b) SEM image of the as-grown crystals and the fracture surface of a pressed pellet, with an intra-granular cracked region outlined in red and an inter-granular cracked region outlined in blue. c) Model of the [$N(CH_3)_4$][$FeBrCl_3$] unit cell with Amm2 structure viewed from the a, b and c axis. Equivalent hydrogen and carbon positions removed for clarity and Br is randomly distributed on Cl sites. d) (010) plane of the unit cell pictured by space filling.

metal halide perovskites are supramolecular structures, as distinct difference is that the perovskites possess a linked network of inorganic octahedra around the organic molecule while the [$N(CH_3)_4$][$FeBrCl_3$] anions do not form such a linked network.[21]

Polycrystalline samples prepared by hot pressing were also analyzed. SEM micrographs of fracture surfaces showed a microstructure that was ceramic-like in appearance with evidence of both inter- and intra-granular brittle fracture (Fig. 1b). Refinement of the pressed material XRD pattern achieved GOF of 2.49 with lattice parameters of a=7.2208 Å, b=8.9894 Å and c=9.3081 Å. By comparison with the crushed crystals, the XRD of pressed pellets showed some degree of structural texturing, evident through the noticeable decreases in the relative intensities of 100, 011 and 020 reflections, and relative increases in the 111 and 102 intensities (Fig. 1a). While the degree of texturing was not quantified, the relative intensities suggests a preferred [111] orientation after pressing. The result demonstrates that it may be possible to manipulate the degree of structural orientation during pressing, which could be highly advantageous for engineering functional properties due to the crystallographic orientation dependence of properties such as the dielectric constant and piezoelectric coefficient.[22–24]

FTIR and Raman spectroscopy were also used to analyze the pressed polycrystalline material (Fig. 2). The Raman spectrum showed features from both the $[FeBrCl_3]^-$ and $[N(CH_3)_4]^+$ molecular ions (Fig. 2a). At low Raman shifts (<400 cm^{-1}), bands were mainly assigned to the vibrational modes

Postprint version of the paper by Walker et al., in J. Mater. Chem. C. vol. 8, Iss. 9, pg. 3206-3216
Doi.org/10.1039/C9TC06918F

from $[FeBrCl_3]^-$ (Fig. 2b).[25–27] The bands at 335, 350 and 395 cm^{-1} are assigned as Fe–Cl stretching modes.[26] The Fe–Br vibrations are most likely responsible for bands at 227, 247, 269 and 294 cm^{-1}, with bands at 227 and 294 cm^{-1} arising due to the asymmetry of the $[FeBrCl_3]^-$ ion.[26] The low intensity band at 206 cm^{-1} is unidentified here, however, we note that it a band at 206 cm^{-1} is observed in the Raman spectrum of $FeBr_4^-$ and may relate to an Fe–Br mode.

Raman shifts at >400 cm^{-1} were assigned to bands from $[N(CH_3)_4]^+$ (Fig. 2a), many of which

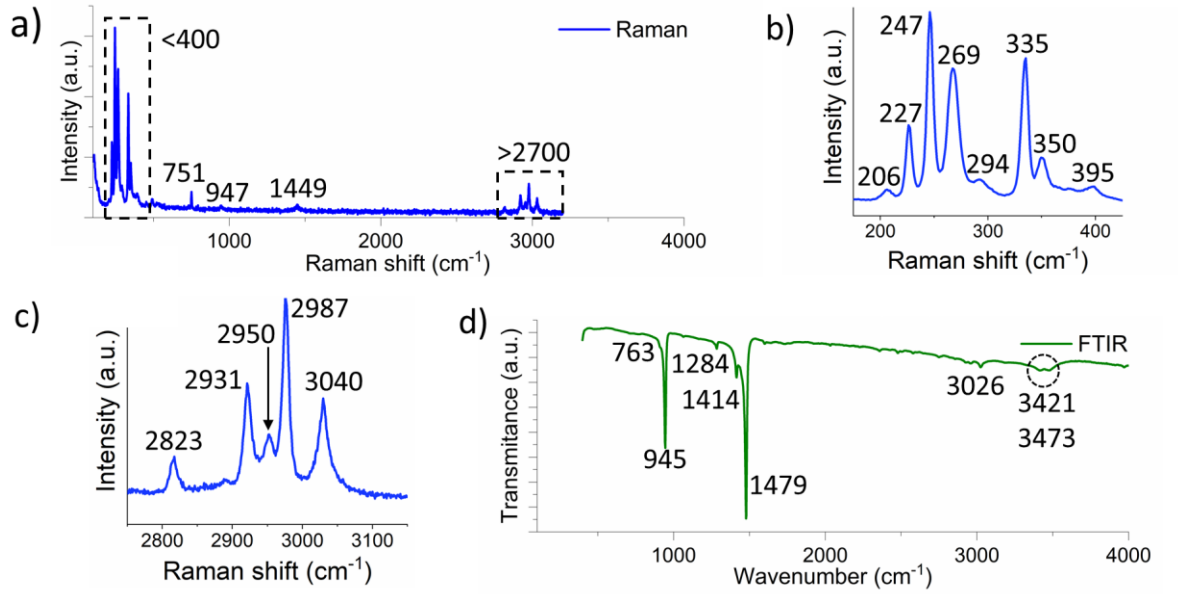

Fig. 2 a) Raman spectrum of $[N(CH_3)_4][FeBrCl_3]$, b) region 150-400 cm^{-1} arising from $[FeBrCl_3]^-$, and c) region 2750-3150 cm^{-1} arising from $[N(CH_3)_4]^+$. d) FTIR spectrum, dashed circle indicates O–H bands.

corresponded to the bands of tetramethylammonium bromide dissolved in water.[28–31] Symmetric and asymmetric stretching bands of C–N were observed at 751 cm^{-1} and 947 cm^{-1}, respectively.[28,31] The band at 1449 cm^{-1} corresponded to the CH_3 bending. The bands between 2700 and 3100 cm^{-1} are mainly assigned to symmetric and asymmetric stretching of C–H (Fig. 3c).[28,30,31]

The FTIR bands in the range 500–4000 cm^{-1} were all assigned to $[N(CH_3)_4]^+$ (Fig. 3d).[30,31] The weak band at 763 cm^{-1} due to A_1 symmetric stretching and the strong band at 945 cm^{-1} due to B_2 asymmetric stretching of C_4N confirmed the C_{2v} perturbation of $[N(CH_3)_4]^+$ in $[N(CH_3)_4][FeBrCl_3]$. The weak band at 1284 cm^{-1} was assigned to the F_2 rocking mode of CH_3 and the bands at 1414, 1479 and 3026 cm^{-1} were assigned to asymmetric deformation of CH_3.

The FTIR spectrum also showed two weak bands at 3421 and 3478 cm^{-1} (indicated by dashed circle in Fig. 2d) which were assigned to O–H stretching modes. The observation of these bands also in organic-inorganic halide perovskite materials exposed to moisture supported this assignation.[32] Thus, here the two bands were considered to identify the presence of water or solvent (ethanol) and likely resulted from incomplete drying after crystallization or adsorption from the ambient environment.

Postprint version of the paper by Walker et al., in J. Mater. Chem. C. vol. 8, Iss. 9, pg. 3206-3216
Doi.org/10.1039/C9TC06918F

Evidence for moisture or ethanol in the material was observed by closer inspection of the microstructure. Higher magnification SEM imaging revealed 1–3 µm sized pores at the grain boundaries (Fig. 3a). The highly spherical shape of the pores and their location exclusively at the grain boundaries led to the conclusion that they were most likely caused by the trapping of liquid vaporized during hot pressing. Crystals dried at 60 °C under vacuum for 6 h before being pressed did not have the same porosity at the grain boundaries (Fig. 3b). A reasonable conclusion was then, that the bands in the FTIR spectrum between 3450 and 3500 cm^{-1} show the presence moisture that was evaporated and trapped at grain boundaries during hot pressing, resulting in the porosity. We note that all subsequent electrical measurements were performed with material prepared by the method of Fig. 3 a) (hot-plate-dried).

Small signal electrical response

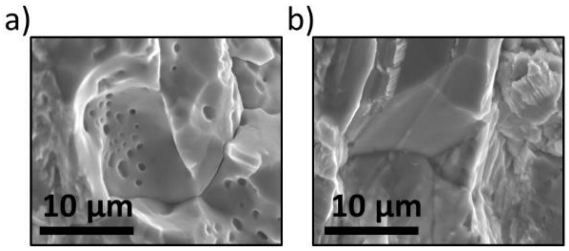

Fig. 3 SEM micrographs of the fracture surface of polycrystalline $[N(CH_3)_4][FeBrCl_3]$ prepared from a) hot-plate-dried, and b) vacuum-oven-dried crystals.

The relative permittivity (ε_r) and loss tangents were measured for pressed pellets of polycrystalline $[N(CH_3)_4][FeBrCl_3]$. At the high frequency 10^6 Hz a ε_r of <20 and a loss tangent of <0.1 was observed (Fig. 4a). The low permittivity may be advantageous for niche applications such as energy harvesting or sensing.[33] However, as the driving field frequency decreased, the ε_r increased to 60 at 10^2 Hz, correlated with a large increase in the dielectric loss to >0.6. The loss tangent showed signs of a weak relaxation at 10^3 Hz and may be related to the presence of inhomogeneity of electrical resistivity in the polycrystalline sample. Due to the loss tangent behavior, the ε_r increase was considered an increase resulting from the extrinsic contributions of electrical loss at lower frequencies.

The polarization-electric field (P-E) hysteresis loops measured at fields of 10 kV/cm showed a characteristic dielectric response with contributions from electrical leakage currents increasing as the driving electric-field frequency was reduced (Fig. 4b).[34–36] At 100 Hz, the loops showed little hysteresis but as the frequency was reduced to 2 Hz the loops became more rounded. Both the low field hysteresis and permittivity data demonstrate the presence of electrical leakage currents. In ferroelectrics high electrical losses originating in the bulk material are usually related to the presence of charged defects related to either lattice vacancies or aliovalent substitutions. In oxide ferroelectrics, for example, oxygen vacancies are the most common site vacancies and play a large role in the electromechanical behavior.[37] Meanwhile in metal halide perovskites the halide species is the most mobile and contributes to the electrical loss via the movement of ions and their reciprocal vacancies.[38] Grain boundaries can also contribute to loss as concentration sites for defects and impurities, such as moisture. The FTIR of $[N(CH_3)_4][FeBrCl_3]$ suggest that moisture was present (Fig. 2), while the porosity in the microstructures suggests that it was present at the grain boundaries (Fig. 3). The moisture could contribute to

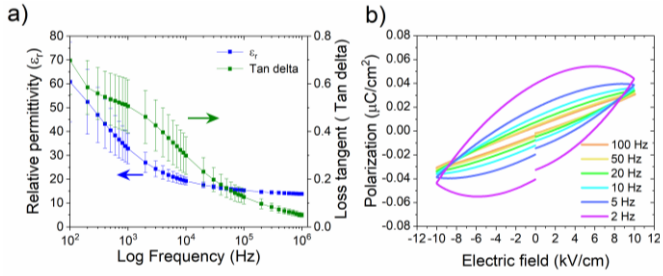

Fig. 4 a) Relative permittivity and loss tangent of $[N(CH_3)_4][FeBrCl_3]$, measured between 10^2 and 10^6 Hz. Error bars show standard deviation determined from three measured samples. b) Polarization-electric field (P-E) hysteresis loops measured at 10 kV/cm between 2 Hz and 100 Hz.

loss behavior by accumulating at grain boundaries, by dissolving the molecular species from $[N(CH_3)_4][FeBrCl_3]$ and creating vacancies in the lattice, or by becoming an interstitial impurity and disturbing the crystal lattice. The precise role is unknown.

Super-coercive electric field hysteresis

The evolution of polarization (P-E), current (I-E) and strain (S-E) hysteresis behavior of $[N(CH_3)_4][FeBrCl_3]$ was observed by sequentially increasing the electric field from 20 to 80 kV/cm with successive field cycles at 10 Hz (Fig. 5a-c). A maximum electric field of 80 kV/cm was chosen as dielectric breakdown occurred at higher electric fields. As the electric field was increased, the P-E loops progressively opened from nearly linear and little hysteretic to square-like with large hysteresis, reminiscent of switching in ferroelectric materials (Fig. 5a). The bloated shape of the P-E loop corners show leakage current contributions which also partly contributed to the apparent remanent polarization (P_r) values that rose from 1.2 to 2.9 $\mu C/cm^2$ between fields of 60 and 80 kV/cm.[36,39] The current-electric field (I-E) hysteresis loops developed what appeared to be ferroelectric switching peaks over the same electric field range, with some noise caused by arching due to the measurements being conducted in air and not an insulating oil (Fig. 5b). The P-E and I-E development coincided with opening of the strain-electric field (S-E) hysteresis loops from minor butterfly-like loops to with peak-to-peak strains (S_{pp}) of 0.019 % at 60 kV/cm, to major butterfly-like shapes with S_{pp} of 0.048 % at 80 kV/cm (Fig. 6c). Some higher frequency noise in the S-E loops was inherent to the measurement set up due to low displacement values (100 nm). S-E loops include all electromechanical contributions to the macroscopic strain, but the butterfly-like shape for ferroelectric materials usually arises due to the significant strain contributions from ferroelastic (non-180°) domain switching and the piezoelectric effect.[37] Therefore, from these hysteresis measurements we infer that the polycrystalline $[N(CH_3)_4][FeBrCl_3]$ materials behave similarly to a typical polycrystalline ferroelectric with some electrical leakage contributions visible in the P-E and I-E loops.

Once the electric field magnitude of 80 kV/cm was reached, further evolution of the hysteresis loops was observed over the first ten cycles at this field (Fig. 5d,e,f). This was a useful exercise to qualitatively observe a phenomenon called wake-up behavior and other electrical contributions.[40] The degree of domain switching saturation refers to the fraction of total ferroelectric domains that switch during each application of electric field, and when additional domains switch with each subsequent cycle this is referred to as wake-up behavior. In the P-E loops, the Pr was observed to increase from 2.9 to 3.8 µC/cm2 with ten further cycles (Fig. 5d). The gap between the start and finishing points of the P-E loops, shown by the dashed circle in Fig. 5d, reduced with increased number of electric field cycles. This can signify a reduced number of new domains switching with each cycle, however, we note that the gap in the P-E loops can also be related with domain back switching between electric field cycles, electrical phenomena such as charge injection, and even instrumental error, so interpretation of the underlying mechanism is not straightforward. The magnitude of the I-E loop peaks increased by nearly 70 % in the first ten cycles, highlighted by the straight arrows in Fig. 5e. A non-linear conductivity component may also be evident in the I-E loops, highlighted by curved arrows in the figure, distinguishable by the curvature of the loops as the electric field decreases from the maximum in both positive and negative field directions.[34–36]

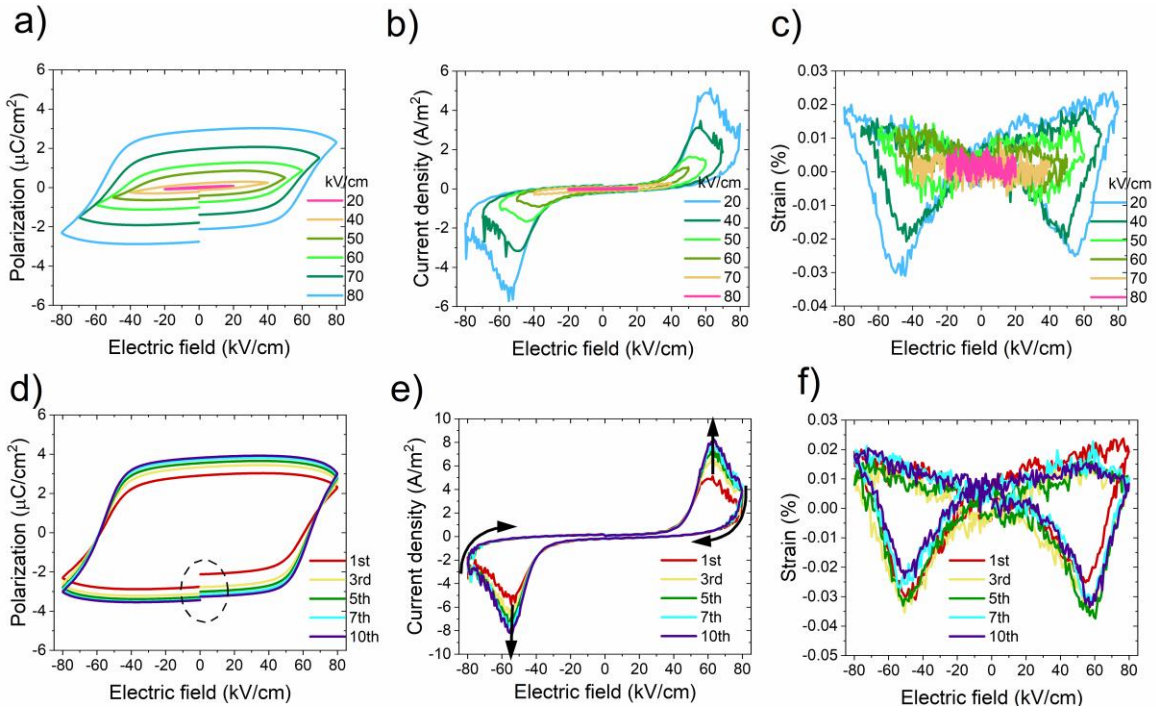

Fig. 5 $[N(CH_3)_4][FeBrCl_3]$ super-coercive hysteresis loops with electric field frequency of 10Hz. a) Polarization, b) current density, and c) strain during increasing electric field from 20 kV/cm to 80 kV/cm, d) polarization, e) current density, and f) strain, during first 10 cycles at electric field of 80 kV/cm. The dashed circle in d) highlights the start and finish points of the P-E loops.

It is important to note that while these observations of wake-up behavior cannot distinguish between the possible contributions from simultaneous increases in electrical leakage and domain switching, they do give a general idea that the switching behavior begins to stabilize over the first 10 cycles at 80 kV/cm. In contrast to the polarization and current, the S_{pp} of the strain loops did not increase with further cycling, instead remaining consistent at 0.046 ± 0.002 % (Fig. 5f). It could then be concluded that electrical mechanisms with no contribution to strain, either increased electrical leakage or increased 180° domain switching, caused the apparent wake-up behavior over the first ten electric field cycles.

Postprint version of the paper by Walker et al., in J. Mater. Chem. C. vol. 8, Iss. 9, pg. 3206-3216
Doi.org/10.1039/C9TC06918F

Frequency dependence of hysteresis

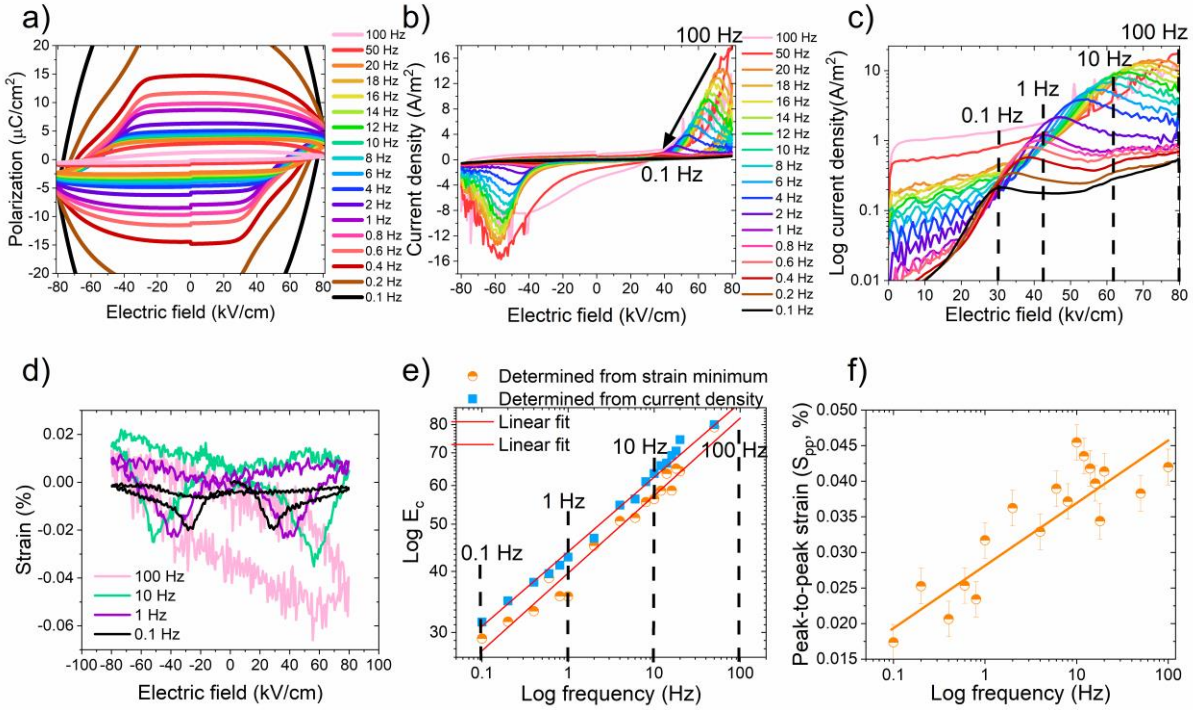

Fig. 6 $[N(CH_3)_4][FeBrCl_3]$ super-coercive ferroelectric switching as a function of frequency from 0.1 Hz to 100 Hz. a) P-E loops and, b) I-E loops. c) I-E loops during increasing of electric field from 0 to 80 kV/cm in the positive field direction with current density on a log scale. d) S-E loops of each frequency decade 0.1, 1, 10, 100 Hz. e) The log E_c as a function of log frequency, determined from the I-E peak and the S-E trough in the positive field direction. Data at 100 Hz is excluded from plot. f) The peak-to-peak (S_{pp}) strain plotted as a function of the applied field frequency. The orange line is guide to for the eye.

Domain switching in ferroelectrics is governed by the time- and field-dependent processes of domain nucleation and growth, and thus is inherently frequency dependent.[41–48] However, extrinsic factors such as interfacial properties, residual stress, chemical defects and structural defects (including grain boundaries) can also have a huge influence on domain switching.[35,49–57] The significant influence of extrinsic factors is perhaps best manifested by the fact that real E_c values determined experimentally from hysteresis measurements are typically much smaller (<10 %) than the intrinsic values predicted by Landau-Ginzburg theory.[45] As a result, the frequency dependence of ferroelectric hysteresis measurements can provide valuable information concerning the domain kinetics and type of extrinsic factors that are dominant in a ferroelectric.

Here the hysteresis behavior of [N(CH3)4][FeBrCl3] was studied at fields of 80 kV/cm between frequencies 100 and 0.1 Hz (Fig. 6). The P-E loops range from sharp loops at 100 Hz indicating the freezing of domain switching, to round or ballooned loops at lower frequencies (<1 Hz), showing strong leakage current contributions (Fig. 6a). The coercive field (Ec) was determined from the median of the I-E peaks in both positive and negative electric field directions (Fig. 6b). The Ec decreased from >80 kV/cm at 100 Hz, to 30 kV/cm at 0.1 Hz. This reduction of Ec with decreasing frequency is highlighted in Fig. 6c where the I-E loops are plotted from 0 to 80 kV/cm as a log of the current density. At 50 and 100 Hz the peak current was reached at 80 kV/cm so Ec is ≥80 kV/cm.

A decrease of E_c with reducing frequency was also observed in the S-E loops where the minimum of the butterfly-like loops in each field direction correlates with the E_c (Fig. 6d).[57] For clarity Fig. 6d only shows the S-E loops at 0.1, 1, 10 and 100 Hz. Loops at 50 (not shown) and 100 Hz did not have

a butterfly-like shape, thus providing no features that were clearly representative of domain switching, similarly as the simultaneously measured I-E loops.

The E_c as a function of frequency observed in both I-E and S-E loops is shown on a log-log plot in Fig. 6e. The coercive field determined from the minimum of the S-E loops in the positive field direction is consistently lower than that determined from current loops. This could be a mark of the complex interaction between leakage currents and domain switching behavior, or alternatively related to the material having distinguishably different E_c for 180 and non-180° domain switching.[58]

Both E_c data sets exhibited an approximately linear relationship up to 50 Hz, with more non-linearity in that determined from the S-E loops. For oxide ferroelectrics, such as $PbZr_{0.2}Ti_{0.8}O_3$, E_c vs frequency log-log plots can exhibit two distinct linear regions with different gradients in a wide enough frequency range.[43–46] These regions signify domain nucleation and domain growth limited switching. We note that only a single gradient is visible in the data in Fig. 6e, but this is not uncommon for bulk samples such as these, as the frequency range is limited and not large enough to see the two distinct regions.[53]

For domain growth limited switching the E_c and frequency relationship can be described using a power law as as $E_c \propto f^{\beta}$, where $\beta = \frac{n}{6}$ and n represents the dimension of domain growth, usually with integer values of 1, 2 or 3.[43,45] The linear fits of each E_c data set here showed gradients of 0.153 and 0.159 for I-E and S-E data sets respectively (red lines in Fig. 6e). Both gradients are marginally smaller than the value of 0.167 that arises from $n = 1$. This signifies that the switching kinetics approximately follow domain growth-limited switching as described by the Kolmogorov-

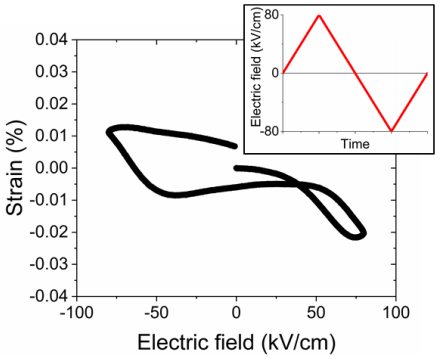

Fig. 7 Strain-electric field hysteresis loop at 100 Hz and 80 kV/cm of a well cycled $[N(CH_3)_4][FeBrCl_3]$ material. Inset shows electric field profile.

Avrami-Ishibashi model.[45]

The magnitude of the peak-to-peak strain (S_{pp}) as a function of frequency is also a useful metric to study and leads to two intriguing observations. Firstly, the S_{pp} reduces as a function of frequency by more than 50 % (Fig. 6f). In ferroelectrics where domain wall de-pinning from point defects or kinetically facilitated ferroelectric switching causes the E_c to decrease with reducing frequency, the S_{pp} often increases.[37,51,59] But interestingly the opposite is observed here.

The second interesting observation is the S_{pp} magnitude and shape at high frequency. At 100 Hz the S-E loop has an oval shape and bears similarities to loops observed in poled ferroelectrics that are cycled at electric fields below their E_c and in the opposite direction to the average polarization direction (Fig. 6c).[51] A similar oval or kidney-like shape is predicted at high frequencies by phase field models based on the time dependent Ginzburg-Landau kinetic equation and is caused by incomplete reversal of the polarization vectors.[41,55] Models show that the effect is exaggerated by internal stress and the volume of the material that is impacted by grain boundaries, which then

introduces a grain size effect. However, contrary to predicted models and observations of the electromechanical response in ferroelectrics with incomplete domain switching, the S_{pp} magnitude is similar to that measured in the butterfly-like loops where domain switching is clearly observed, i.e. 0.046 % at 10 Hz. This is unusual as the ferroelastic switching component of strain, including domain wall motion, often contributes the largest fraction of total strain to butterfly-like hysteresis.[59]

The frequency dependent hysteresis results show that while the S-E shape at 100 Hz may be an effect of driving the samples just below the E_c and achieving incomplete polarization reversal, the frequency dependent S-E magnitude suggests that the electromechanical response of $[N(CH_3)_4][FeBrCl_3]$ is complicated and may involve mechanisms in addition to those most common in oxide ferroelectrics, that is, ferroelastic switching and the piezoelectric effect. It is important to note that the effect of grain boundaries, and thus the role of grain size, on the frequency dependence of hysteresis in plastic crystal ferroelectrics is currently unknown. However, the grain size in these materials, approximated from the as grown crystals, is several orders of magnitude larger than the grain size range in which grain size effects are significant in oxide ferroelectrics.[36,41,55] As well as this, the kinetic coefficient for polarization reversal has not yet been studied, nor the impact of stress. For this reason, there is tremendous room for further investigation of switching dynamics in these ferroelectric materials.

Asymmetry of the electromechanical response

To establish a greater understanding of the electromechanical properties and mechanisms, the strain hysteresis was measured during successive cycles at 100 Hz, with opposite electric field

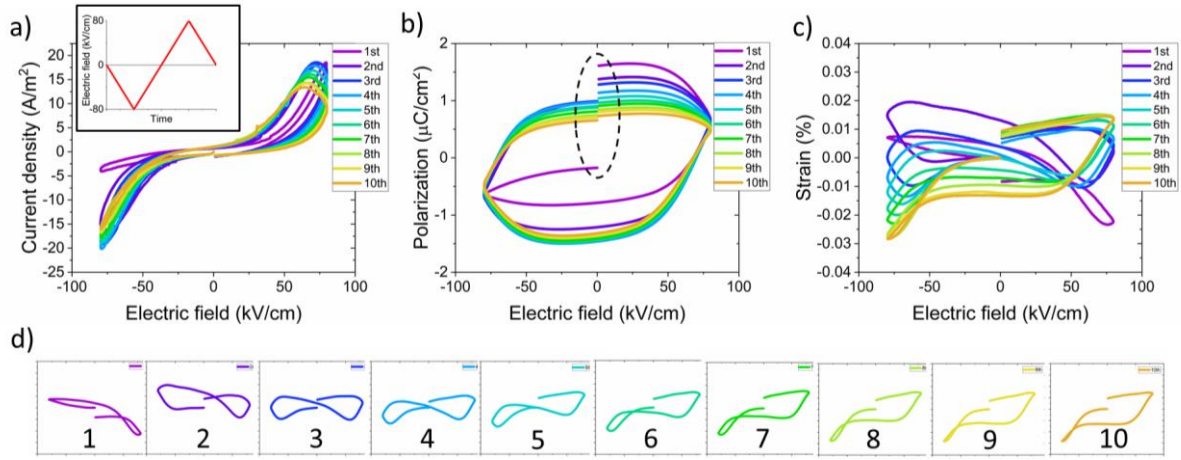

Fig. 8 Consecutive hysteresis loop measurements made on a well cycled sample of $[N(CH_3)_4][FeBrCl_3]$ after reversing the field direction from positive to negative. a) Current density, inset shows electric field profile, b) polarization, c) strain, and d) strain for each field cycle plotted separately, with cycle number.

directions described as follows.

First a sample was taken through the wake-up process of systematically increasing the electric field with each successive cycle from 0 to 80 kV/cm at 10 Hz. Once at 80 kV/cm, the field frequency was increased to 100 Hz and the sample was cycled 10 times with the field first becoming positive and then negative (Fig. 7 inset). In this state, the sample exhibited a strongly asymmetric hysteresis most evident in the S-E loop (Fig. 7). The asymmetric shape exhibits more complete switching (meaning more butterfly-like shape) in the negative field direction and less complete switching in the positive field direction.

The polarity of the applied electric field direction was then reversed, with the first half of the field cycle being negative and the second half positive (inset Fig. 8a). Over the next 10 cycles a reversal

of the asymmetric shape was observed (Fig. 8). The I-E loops evolved, developing a broad peak below the maximum electric field in the positive field region, and a peak at the maximum field in the negative electric field direction (Fig. 8a). The P-E loops first showed a large gap between the starting and finishing points, which reduced over successive cycles (shown with a dashed circle in Fig. 8b). In the S-E loops, the asymmetric shape progressively reversed with respect to electric field with each successive cycle, going through a symmetric shape after 3 cycles (Fig. 8c,d). The evolution slowed down, approaching an apparent finite limit of asymmetry, so that loops from field cycles 10 to 15 (not shown) exhibited little difference.

The electric field direction was then reversed again (Fig. 9). Over a further 10 cycles the I-E loop shape reverse sequentially (Fig. 9a). The P-E loops again evolved to close a gap between the start and finish points of the loop (shown by the dashed circle Fig. 9b), and the I-E shape began to reverse with respect to electric field (Fig. 9c,d). The shape evolution on this second reversal of electric field was slower, with the symmetric S-E shape not occurring until the 6th cycle and the asymmetry being generally less pronounced by the 10th cycle (Fig. 9d).

Asymmetric hysteresis behavior during bipolar electric field cycling has previously been attributed to the orientation and formation of defect dipole complexes in ferroelectrics. Hysteresis asymmetry is common among materials referred to as “hard” ferroelectrics, such as Fe doped Pb(Zr,Ti)O_3 and BiFeO3, and is usually caused by defect pinning.[61–65] Defect pinning is the result of point defects being distributed to produce an internal bias field that interferes with domain wall movement.[49] The hysteresis asymmetry is usually most apparent before a saturated domain switching state is reached and can change over time and number of electric field cycles, depending on the mobility of the point defects. In $[N(CH_3)_4][FeBrCl_3]$, the reversibility of hysteresis asymmetry with respect to the electric field direction tells us that that the mechanism for hysteresis asymmetry is electrically activated. While the frequency dependence of the electric field hysteresis behavior (as shown in Fig. 6) demonstrates that the mechanism behind the asymmetry possesses slower kinetics than ferroelectric/ferroelastic domain switching. These two observations are consistent with a defect pinning model, but do not exclude the possibility of other mechanisms, such as grain size effects or small domain switching kinetic coefficients. We do note however, that while some similar supramolecular ferroelectrics do exhibit some frequency dependent hysteresis, switching was achieved at frequencies in excess of 1 kHz, an order of

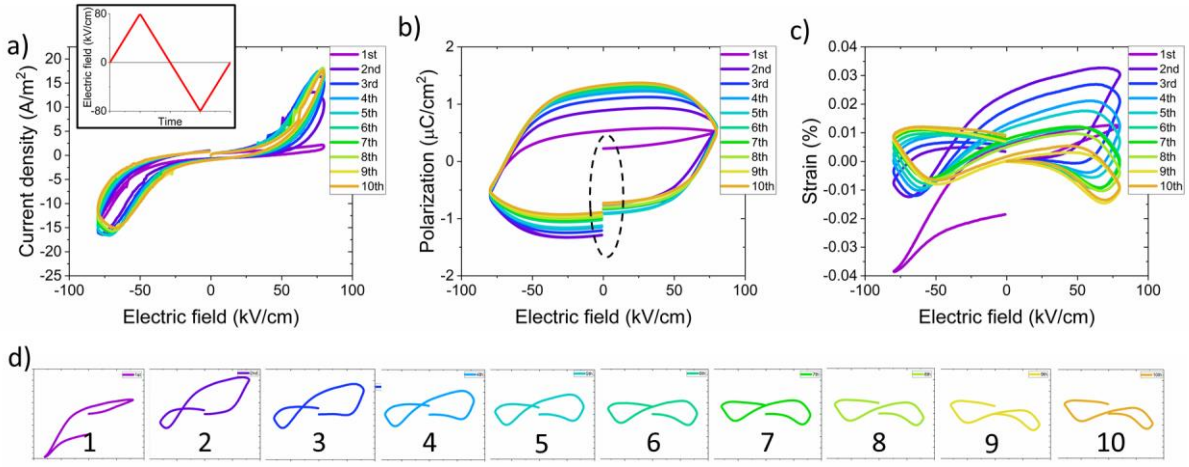

Fig. 9 Consecutive hysteresis loop measurements made on sample of $[N(CH_3)_4][FeBrCl_3]$ in the positive field direction after measurements in (Fig. 8). a) Current density, inset shows electric field profile, b) polarization, c) strain, and d) strain for each field cycle plotted separately, with cycle number.

magnitude higher than that observed here.[66–68] Hence we think the role of extrinsic effects, such as charged defects, is likely in the materials observed here.

Using a defect pinning model, the gradual reversibility of the asymmetry in $[N(CH_3)_4][FeBrCl_3]$ may be explained by point defects being mobile under electric field. The presence of an internal bias field is evident in the 10th cycle Fig. 8b by the different E_c observed in the positive (68 kV/cm) and negative (-72 kV/cm) electric field directions, giving an internal bias field of -4 kV/cm. The bias field in Fig. 9b after the 10th cycle was +4 kV/cm, showing that when the electric field is reversed the bias field also reverses.

The synthesis process and the FTIR data provide information about the possible sources of point defects in the $[N(CH_3)_4][FeBrCl_3]$. The iron trichloride hexahydrate precursor is hygroscopic, meaning that an undetermined mass of water was present during the weighing of iron trichloride hexahydrate powders resulting in the solution being deficient in $[FeCl_3]$. This non-stoichiometry is expected to produce $[N(CH_3)_4][FeBrCl_3]$ crystals with $[FeBrCl_3]^-$ vacancies ($V^{\bullet}_{[FeBrCl3]}$ in Kröger-Vink notation), charge balanced by disassociated Br^- ions. The Br^- may be included as either interstitial Br_i' or as a substitutional $Br'_{[FeBrCl3]}$ at the anion site in the crystal lattice. Both scenarios are plausible because of the small ionic radius of Br^- (1.96 Å) relative to the crystal lattice parameters (on the order of 10 Å). The literature also suggests that the halide species, such as Br^-, are likely mobile under an electric field, analogous to O^{2-} in metal oxide ferroelectrics, and this could also play a role in the systematic evolution of hysteresis asymmetry observed here.[38] In addition, the FTIR data (Fig. 2) shows the presence of moisture (H_2O). It is thus, plausible that H_2O also plays a role in the observed behavior, either as an interstitial impurity creating a point defect in the structure, or as a solvent for the molecular ions at grain boundaries. Therefore, the data suggests that the four types of point defects $V^{\bullet}_{[FeBrCl3]}$, $Br'_{FeBrCl3}$, Br_i', and H_2O_i are likely present within the $[N(CH_3)_4][FeBrCl_3]$ crystal lattice and could be involved in both the frequency dependence and the reversible asymmetry observed in the hysteresis.

Conclusions

The polycrystalline $[N(CH_3)_4N][FeBrCl_3]$ with the non-centrosymmetric structure *Amm*2 was fabricated by crystallization from solution and hot pressing at 150 °C. The materials exhibited a ferroelectric like hysteresis behavior at the driving electric field frequency of 10 Hz, with some wake-up behavior typical of many ferroelectrics, achieving a P_r of 3.8 μC/cm^2 and S_{pp} of 0.046 % at a field of 80 kV/cm. The hysteresis behavior exhibited a strong frequency dependence at driving electric field frequencies between 0.1 and 100 Hz and at 100 Hz the loops were strongly asymmetric. This asymmetry was reversible under opposite driving electric field directions. Meanwhile, the dielectric loss tangent and permittivity showed contributions from electrical leakage, evident by increased values at frequencies below 10^6 Hz. The high losses, frequency dependence and reversible asymmetry evident in the electrical measurements showed an intriguing fingerprint consistent with defect pinning. In a defect pinning model the mobility of point defects present in the material produce an internal bias field that interferes with domain switching. Two plausible sources of point defects in the $[N(CH_3)_4][FeBrCl_3]$ crystal were non-stoichiometry resulting in $V^{\bullet}_{[FeBrCl3]}$ and Br_I', $Br'_{FeBrCl3}$ or moisture (H_2O), the latter was supported by the presence of O–H stretching bands identified with FTIR.

This study sheds light on type of defects and the role they may play in the dielectric, ferroelectric/ferroelastic domain switching and electromechanical properties of ferroelectric plastic crystals and other emerging hybrid organic-inorganic supramolecular ferroelectrics. It highlights the need for a further investigation of domain switching kinetics from intrinsic growth and nucleation processes to the extrinsic influences like grain boundaries and defects.

Postprint version of the paper by Walker et al., in J. Mater. Chem. C. vol. 8, Iss. 9, pg. 3206-3216
Doi.org/10.1039/C9TC06918F

Conflicts of interest

There are no conflicts to declare.

Acknowledgements

JW acknowledges the financial contribution of NTNU. TR would like to thank the Slovenian Research Agency for providing funding within the programme P2-0105 and NAMASTE center of excellence.

References

1 G. H. Haertling, J. Amer. Ceram. Soc., 1999, **82**, 797-818.
2 D. Damjanovic, Reps. Prog. Phys., 1998, **100**, 1267-1324.
3 K. S. Ramadan, D. Sameoto, S. Evoy, Smart Mater. Struct., 2014, **23**, 033001-26.
4 A. H. King, Nature Mater., 2019, **18**, 408-409.
5 T. Ibn-Mohammed, C. A. Randall, K. B. Mustapha, J. Guo, J. Walker, S. Berbano, S. C. L. Koh, D. Wang, D. C. Sinclair, I. M. Reaney, J. Euro. Ceram. Soc., 2019, **39**, 5213-5235.
6 S. Horiuchi, Y. Tokura, Nature Mater., 2008, **7**, 357-366.
7 J. Harada, T. Shimojo, H. Oyamaguchi, H. Hasegawa, Y. Takahshi, K. Satomi, Y. Suzuki, J. Kawamata, T. Inabe, Nature Chem., 2016, **8**, 946-952.
8 Y.-M. You, Y.-Y. Tang, P.-F. Li, H.-Y. Zhang, W.-Y. Zhang, Y. Zhang, H.-Y. Ye, T. Nakamura, R.-G. Xiong, Nature Commun., 2017, **8**, 14934-7.
9 J. Harada, N. Yoneyama, S. Yokokura, Y. Takahashi, A. Miura, N. Kitamura, T. Inabe, J. Amer. Chem. Soc., 2018, **140**, 346-354.
10 D. Li, X.-M. Zhao, H.-X. Zhao, L.-S. Long, L.-S. Zheng, Inorg. Chem., 2019, **58**, 655-662.
11 Q. Pan, Z. -B. Liu, H. -Y. Zhang, W. -Y. Zhang, Y. -Y. Tang, Y. -M. You, P. -F. Li, W. -Q. Liao, P. -P. Shi, R. -W. Ma, R. -Y. Wei, R. -G. Xiong, Adv. Mater., 2017, **29**, 1700831-7.
12 J. Timmermans, J. Phys. Chem. Solids, 1961, **18**, 1-8.
13 J. M. Pringle, P.C. Howlett, D. R. MacFarlane, M. Forsyth, J. Mater. Chem., 2010, **20**, 2056-2062.
14 Y. -Y. Tang, P.-F. Li, W. -Q. Liao, P. -P. Shi, Y.-M. You, R. -G. Xiong, J. Am. Chem. Soc., 2018, **140**, 8051-8059.
15 S.-G. Kim, S. Priya, I. Kanno, MRS Bulletin, 2012, **37**, 1039-1050.
16 C. R. Bowen, A. A. Kim, P. M. Weaver, S. Dunn, Energy Environ. Sci., 2014, **7**, 25-44.
17 J. W. Lauher, J. A. Ibers, Inorg. Chem., 1975, **14**, 348-351.
18 Z. Czapla, O. Czupinski, Z. Galewski, L. Sobczyk, Solid Stat. Commun., 1985, **56**, 741-72.
19 D. Wyrzykowski, R. Kruszynski, J. Klak, J. Mrozinski, Z. Warnke, Inorg. Chem. Acta, 2008, **361**, 262-268.
20 J. Salgado-Beceiro, S. Castro-Garcia, M. Sanchez-Andujar, F. Rivadulla, J. Phys. Chem. C., 2018, **122**, 27769-27774.
21 D. A. Egger, A. M. Rappe, L. Kronik, Acc. Chem. Res., 2016, **49**, 573-581.
22 M. Deluca, Adv. Appl. Ceram., 2016, **115**, 112-122.
23 J. L. Jones, B. J. Iverson, K. J. Bowman, J. Am. Ceram. Soc., 2007, **90**, 2297-2314.
24 H. G. Yeo, T. Xue, S. Rundy, X. Ma, C. Rahn, S. Trolier-McKinstry, Adv. Funct. Mater., 2018, **28**, 1801327-9.
25 Q. Zhao, T. S. Herng, C. X. Guo, D. Zhao, J. Ding, X. Lu, RSC Adv., 2016, **6**, 15731-15734.
26 M. Doebbelin, V. Jovanovski, I. Llarena, L. J. Claros Marfil, G. Cabanero, J. Rodriguez, D. Mecerreyes, Polym. Chem., 2011, **2**, 1275–1278.

27 M. C. Smith, Y. Xiao, H. Wang, S. J. George, D. Coucouvanis, M. Koutmos, W. Sturhahn, E. E. Alp, J. Zhao, S. P. Cramer, Inorg. Chem., 2005, **44**, 5562-5570.
28 E. Spinner, Spectrochimica Acta Part A., 2003, **59**, 1441-1456.
29 Y. Ren, X. Cheng, K. Yang, X. Zhu, H. Li, Y. Wang, J. Molecul. Struct., 2015, **1102**, 6-10.
30 M. Abul Hossain, F. Ahmed, J. P. Srivastava, Phys. Stat. Sol. (a), 1995, **151**, 299-304.
31 V. I. Torgashev, Y. I. Yuzyuk, L. M. Rabkin, Y. I. Durnev, L. T. Latush, Phys. Stat. Sol. (b), 1991, **165**, 305-318.
32 J. Idigoras, A. Todinova, J. R. Sanchez-Valencia, A. Barranco, A. Borras, J. A. Anta, Phys. Chem. Chem. Phys., 2016, **18**, 13583-13590.
33 P. Muralt, Integrat. Ferro., 1997, **17**, 297-307.
34 G. Liu, S. Zhang, W. Jiang, W. Cao, Mater. Sci. Eng. R. Rep., 2015, **89**, 1-48.
35 L. Jin, F. Li, S. Zhang, J. Am. Ceram. Soc., 2014, **97**, 1-27.
36 H. Yan, F. Inam, G. Viola, H. Ning, H. Zhang, Q. Jiang, T. Zeng, Z. Gao, M. J. Reece, J. Adv. Dielec., 2011, **1**, 107-118.
37 D. Damjanovic, "Hysteresis in piezoelectric and ferroelectric materials," in Science of Hysteresis, edited by G. Bertotti and I. Mayergoyz, Oxford, Academic Press, 2006, Vol. III, pp. 337–465.
38 Y. Yuan, J. Huang, Acc. Chem. Res. 2016, **49**, 286-293.
39 T. Schenk, E. Yurchuk, S. Mueller, U. Schroeder, S. Starschich, U. Bottger, T. Mikolajick, Appl. Phys. Rev., 2014, **1**, 041103-14.
40 J. Walker, H. Simons, D. O. Alikin, A. P. Turygin, V. Y. Shur, A. L. Kholkin, H. Ursic, A. Bencan, B. Malic, V. Nagarajan, T. Rojac, Sci. Reps. 2016, **6**, 19630-8.
41 Y. Su, N. Liu, G. J. Weng, Acta Mater., 2015, **87**, 293-308.
42 S. Ducharme, V. M. Fridkin, A. V. Bune, S. P. Palto, L. M. Blinov, N. N. Petukhova, S. G. Yudin, Phys. Rev. Lett., 2000, **84**, 175
43 D. Vieland, Y.-H. Chen, J. Appl. Phys., 2000, 88, 6696-6707.
44 A. N. Morozovska, E. A. Eliseev, S. L. Bravina, S. V. Kalinin, J. Appl. Phys., 2011, 110, 052011-9.
45 W. Li, Z. Chen, O. Auciello, J. Phys. D: Appl. Phys., 2011, 44, 105404-6.
46 H. Orihara, S. Hashimoto, Y. Ishibashi, J. Phys. Soc. Jpn., 1994, 63, 1031-1035.
47 Y. W. So, D. J. Kim, T. W. Noh, J.-G. Yoon, T. K. Song, Appl. Phys. Lett. 2005, 86, 0902905-3.
48 A. K. Tagantsev, I. Stolichnov, N. Setter, J. S. Cross, M. Tsukada, Phys. Rev. B., 2002, 66, 214109-6.
49 U. Robels, G. Arlt, J. Appl. Phys., 1993, **73**, 3454-7.
50 M. H. Lente, A. Picinin, J. P. Rino, J. A. Eiras, J. Appl. Phys., 2004, **95**, 2646.
51 T. Rojac, M. kosec, D. Damjanovic, J. Am. Ceram. Soc., 2011, **94**, 4108-4111.
52 A. Ruff, Z. Li, A. Loidi, J. Schaab, M. Fiebig, A. Cano, Z. Yan, E. Bourret, J. Glaum, D. Meier, S. Krohns, Appl. Phys. Lett., 2018, **112**, 182908-5.
53 R. Yimnirun, Y. Laosiritaworn, S. Wongsaenmai, S. Ananta, Appl. Phys. Lett., 2006, **89**, 162901-3.
54 Y. Tan, J. Zhang, Y. Wu, C. Wang, V. Koval, B. Shi, H. Ye, R. McKinnon, G. Viola, H. Yan, Sci. Reps., 2015, 5, 9953-9.
55 Y. Su, H. Kang, Y. Wang, J. Li, G. J. Weng, Phys. Rev. B., 2017, 95, 054121-12.
56 L. M. Denis, G. Esteves, J. Walker, J. L. Jones, S. Trolier-McKinstry, Acta Mater., 2018, 151, 243-253.
57 S. C. Hwang, C. S. Lynch, R. M. McMeeking, Acta Metall. Mater., 1995, **43**, 2073-2084.
58 N. Uchida, T. Ikeda, Jap. J. Appl. Phys., 1965, **4**, 867-880.
59 J. E. Daniels, T. R. Finlayson, J. Appl. Phys., 2007, **101**, 104108-7.
60 T. Tsurumi, Y. Kumano, N. Ohashi, T. Takenaka, O. Fukunaga, Jpn. J. Appl. Phys., 1997, **36**, 5970-5975.
61 B. Jaffe, W. R. Cook, H. Jaffe, *Piezoelectric ceramics*, Academic press, London and New York, 1971.
62 D. Berlincourt, J. Acoust. Soc. Am., 1992, **91**, 3034-40.

63 C. Jullian, J. F. Li, D. Vieland, J. Appl. Phys., 2004, **95**, 4316-3.
64 T. Rojac, H. Ursic, A. Bencan, B. Malic, D. Damjanovic, Adv. Funct. Mater., 2015, **25**, 2099-2108.
65 Y. A. Genenko, J. Glaum, M. J. Hoffman, K. Albe, Mater. Sci. Eng. B., 2015, **192**, 52-82.
66 W.-J. Xu, P.-F. Li, Y.-Y. Tang, W.-X. Zhang, R.-G. Xiong, X.-M. Chen, J. Am. Chem. Soc., 2017, **139**, 6369-6375.
67 Y.-Y. Tang, P.-F. Li, W.-Q. Liao, P.-P. Shi, Y.-M. You, R.-G. Xiong, J. Am. Chem. Soc. 2018, **140**, 8051-8059.
68 J. Harada, Y. Kawamura, Y. Takahashi, Y. Uemura, T. Hasegawa, H. Taniguchi, K. Maruyama, J. Am. Chem. Soc., 2019, **141**, 9349-9357.